

The Study of Dust Formation of Four Type Ibn Supernovae

WEN-PEI GAN,¹ SHAN-QIN WANG,¹ AND EN-WEI LIANG¹

¹*Guangxi Key Laboratory for Relativistic Astrophysics, School of Physical Science and Technology, Guangxi University, Nanning 530004, China*

(Published in ApJ on June 23, 2021)

ABSTRACT

In this paper, we investigate the early-time optical–near-infrared (NIR) spectral energy distributions (SEDs) of four Type Ibn supernovae (SNe). We find that the SEDs of SN 2010al, LSQ13ddu, and SN 2015G can be well explained by the single-component blackbody model, while the SEDs of OGLE-2012-SN-006 cannot. We invoke the double-component model assuming that the SEDs were produced by the SN photosphere and the heated dust to fit the optical–NIR SEDs of the four SNe Ibn, finding that the derived temperatures of the dust associated with OGLE-2012-SN-006 favor the scenario that the dust consists of the graphite grains, and the mass and temperature of dust are $\sim 0.5\text{--}2.0 \times 10^{-3} M_{\odot}$ and $\sim 1200\text{--}1300$ K, respectively. Moreover, our fits for SN 2010al, LSQ13ddu, and SN 2015G show that the upper limits of the masses of the dust associated with the three SNe Ibn are respectively $1.45 \times 10^{-5} M_{\odot}$, $5.9 \times 10^{-7} M_{\odot}$, and $2.4 \times 10^{-7} M_{\odot}$. A further analysis demonstrates that the inferred radius of the dust shell surrounding OGLE-2012-SN-006 is significantly larger than that of the SN ejecta at early epochs, indicating that the NIR excesses of the SEDs of OGLE-2012-SN-006 were produced by a preexisting dust shell. Our study for the early-time SEDs of four SNe Ibn, together with the previous studies and the fact that some SNe showed the evidence of dust formation at the late-time SEDs, indicates that at least $\sim 1/3$ of SNe Ibn show evidence for dust formation.

Keywords: Circumstellar matter (241); Supernovae (1668)

1. INTRODUCTION

Type Ibn supernovae (SNe Ibn; Pastorello et al. 2016; Hosseinzadeh et al. 2017) are believed to be produced by a massive star surrounded by a dense helium-rich circumstellar material (CSM) that can be either winds blown by the SN progenitors or shells expelled by the progenitors (Foley et al. 2007; Pastorello et al. 2007). In this scenario, the interaction between the SN ejecta and the CSM produces forward shocks and reverse shocks. The forward shocks ionized the helium-rich CSM, which can emit narrow- and/or intermediate-width emission lines when the ionized helium recombine.

Assuming the ratio of the dust mass to the gas mass is 1:100 which is a standard value (e.g., Tartaglia et al. 2020), there must be a moderate mass of dust surrounding the progenitor of an SN Ibn before the SN explosion. Alternatively, the ejecta–CSM interaction might produce new dust in the shocked regions. The UV and optical photons from the SNe would heat the preexisting and/or new dust, then the heated dust would yield excess emission peaking at near infrared (NIR) or middle-IR (MIR).

Therefore, the IR excesses at the early epochs and/or the IR detections at the (very) late epochs can provide useful information for exploring the dust formation associated with an SN.

To date, at least a few dozen SNe have been confirmed to be surrounded by a moderate amount ($\sim 10^{-6}\text{--}10^{-2} M_{\odot}$; see, e.g., Fox et al. 2011, 2013; Szalai et al. 2019) of dust. For comparison, only one SN Ibn (SN 2006jc) was previously found to have evidence of dust formation (Mattila et al. 2008; Smith et al. 2008).

It is an interesting issue to search for the evidence of dust formation associated with other SNe Ibn. One of prevailing methods confirming the dust formation associated with SNe is studying the optical and NIR/MIR spectral energy distributions (SEDs) of the SNe since the dust emission would yield IR excesses.

So far, only six SNe Ibn (SN 2010al, Pastorello et al. 2015a; OGLE-2012-SN-006, Pastorello et al. 2015b; SN 2006jc, Foley et al. 2007; Smith et al. 2008; Pastorello et al. 2008; Tominaga et al. 2008; PS1-12skm, Sanders et al. 2013; Hosseinzadeh et al. 2019; LSQ13ddu, Clark et al. 2020; SN 2015G Shivvers et al. 2017; Hosseinzadeh et al. 2017) have been observed in both optical and NIR (*JHK*) bands. Among these six SNe Ibn, as mentioned above, SN 2006jc was previously found to have SEDs showing NIR excesses from dust that had been interpreted by a two-component model assuming that the NIR excesses were produced by the preexisting dust (Dwek 1985) in the CSM and/or the newly formed dust in the shocked CSM (Mattila et al. 2008; Smith et al. 2008). In contrast, Sanders et al. (2013) point out that the SEDs of PS1-12sk do not show significant NIR excess (see their Figure 4).

The evidence for dust formation in the remaining four SNe Ibn with optical and NIR data had not been studied. In this paper, we study the SEDs of the four SNe Ibn (SN 2010al, OGLE-2012-SN-006, LSQ13ddu, and SN 2015G) that have *JHK* photometry but have not been studied in detail. In section 2, we use the single-component model and double-component model to fit the SEDs of the four SNe Ibn. We discuss our results and draw conclusions in Sections 3 and 4, respectively.

2. THE OPTICAL AND NIR SEDS AND THE SED FITTING

In this section, we study the SEDs of four SNe Ibn (SN 2010al, OGLE-2012-SN-006, LSQ13ddu, and SN 2015G) whose details are listed in Table 1. The redshifts (z) of the SNe in the sample are between 0.005 and 0.06, and the observations for the sample cover both the optical and the NIR bands.

First, we fit the SEDs of the SNe Ibn using the single-component model, which assumes that the SEDs are produced by the blackbody emission from the SN photosphere,

$$F_{\nu,\text{ph}} = \pi B_{\nu}(T_{\text{ph}}) \frac{R_{\text{ph}}^2}{D_L^2}, \quad (1)$$

where $F_{\nu,\text{ph}}$ and $B_{\nu}(T_{\text{ph}}) = (2h\nu^3/c^2)(e^{\frac{h\nu}{k_b T_{\text{ph}}}} - 1)^{-1}$ are the flux and the intensity of the blackbody radiation of the SN photosphere, respectively. R_{ph} , T_{ph} , and D_L are the radius, temperature of the SN photosphere, and the luminosity distance of the SN, respectively.

To get best-fitting parameters and the 1σ range of the parameters, we adopt the Markov Chain Monte Carlo (MCMC) method by using the `emcee` Python package (Foreman-Mackey et al. 2013). The best-fitting theoretical SEDs of these four SNe Ibn are shown in Figure 1.

It can be found that the SEDs of SN 2010al, LSQ13ddu, and SN 2015G can be well explained by the single-component blackbody model, indicating that there is no significant evidence of the dust formation associated with these three SNe.

In contrast, the SEDs of OGLE-2012-SN-006 cannot be explained by this model since the SEDs show evident NIR (*JHK*) excesses. To account for the NIR (*JHK*) excesses of the SEDs of OGLE-2012-SN-006 and constrain the upper limits of the dust masses associated with SN 2010al, LSQ13ddu, and SN 2015G, a two-component model is needed. This model assumes a portion of the UV and optical flux produced in the ejecta of SNe heats the dust shells and the heated dust emits IR photons, producing the IR excesses (Dwek 1983). Hence, we employ the double-component model assuming that the flux is the sum of the emission of SN photosphere and the dust shell.

The total flux of the two-component model can be written as

$$F_{\nu} = F_{\nu,\text{ph}} + F_{\nu,\text{d}} \quad (2)$$

where the first component is from the SN photosphere and described by Equation (1), while the second component, which is from the heated dust, can be expressed as (Hildebrand 1983)

$$F_{\nu,\text{d}} = B_{\nu}(T_{\text{d}}) \frac{M_{\text{d}} \kappa_{\nu}(a)}{D_L^2}, \quad (3)$$

Here, $F_{\nu,\text{d}}$ is the flux from the dust shell, $B_{\nu}(T_{\text{d}}) = (2h\nu^3/c^2)(e^{\frac{h\nu}{k_b T_{\text{d}}}} - 1)^{-1}$ is the intensity of the black-body radiation of a dust grain, and M_{d} is the mass of the dust shell.

The mass absorption coefficient ($\kappa_\nu(a)$) of the dust grains plays a crucial role in the model. Following Dwek (1983), $\kappa_\nu(a)$ can be written as

$$\kappa_\nu(a) = \frac{3Q_\nu(a)}{4\rho a}, \quad (4)$$

where ρ and a are the mass density and radius of the spherical dust grain, respectively. Fixing the values of ρ and a , $\kappa_\nu(a)$ is uniquely determined by the value of the emission efficiency $Q_\nu(a)$, which can be calculated by Mie theory for the dust grains. As suggested by previous studies (e.g., Laor & Draine 1993; Fox et al. 2010, 2011; Stritzinger et al. 2012), the grains in the dust shell surrounding SNe can be either graphite or silicate whose mass densities are 2.26 g cm^{-3} and 3.3 g cm^{-3} , respectively (Laor & Draine 1993).

Using Mie theory, we plot in Figure 2 the emission efficiencies ($Q_\nu(a)$) for both graphite and silicate. The data of the refractive index and the extinction coefficient of graphite and silicate needed for our calculations are from Draine (2003) which are presented in Draine’s website.¹ For comparison, we overplot the emission efficiency curves using the data downloaded from Draine’s website where the data were yielded by using the equations listed in Draine & Lee (1984) and Laor & Draine (1993).² For silicate, the two groups of curves are consistent with each other. For graphite, the two groups of curves are slightly different if λ is $\lesssim 5 \times 10^{-3} \mu\text{m}$ or $\gtrsim 10 \mu\text{m}$. The discrepancy is due to the fact that the curves of $Q_\nu(a)$ from Draine’s website is based on the refractive index and the extinction coefficient from Laor & Draine (1993) while the curves of $Q_\nu(a)$ we calculate are based on the refractive index and the extinction coefficient from Draine (2003). Nevertheless, the discrepancy is irrelevant since the range of the effective wavelength of the NIR bands (*JHK*) is $\sim 1.2 - 2.2 \mu\text{m}$.

In principle, the radius of the dust grains a can be included in the MCMC; however, the fitting for SEDs of different epochs might result in different a while a ought to be a constant at different epochs for the same SN. Here, we assume that $a = 0.10 \mu\text{m}$. So the free parameters of the double-component SED fitting are R_{ph} , T_{ph} , T_{d} , and M_{d} .

The SEDs of the four SNe Ibn at all epochs can be well explained by the double-component model (see Figure 3); the corresponding corner plots (for graphite dust) are shown in Figures A1, A2, A3, and A4. The best-fitting parameters of the two-component model are presented in Table 2. We note that the model fits for late-time SEDs are not very well. This is because the simple double-component model must yield smooth theoretical SEDs that cannot fully match the observed SEDs that have undulation features. Nevertheless, the slight deviations between the theoretical two-component SEDs and the observed ones are within a reasonable range.

The derived temperatures can be used to judge the composition of the dust. The evaporation temperatures of silicate and graphite are $\sim 1100\text{-}1500 \text{ K}$ (e.g., Laor & Draine 1993; Mattila et al. 2008; Gall et al. 2014) and $\sim 1900 \text{ K}$ (e.g., Stritzinger et al. 2012), respectively. Comparing these two values to the best-fitting temperatures of the silicate and graphite, we find the former can be excluded and the latter is favored.

For OGLE-2012-SN-006, the best-fitting values of T_{ph} , R_{ph} , T_{d} and M_{d} at different epochs are $\sim 6400 - 7800 \text{ K}$, $\sim 0.9 - 1.9 \times 10^{15} \text{ cm}$, $\sim 1200 - 1300 \text{ K}$, and $\sim 0.5 - 2.0 \times 10^{-3} M_{\odot}$, respectively. It should be noted that the inferred mass of the dust is just a lower limit since the dust grains with lower temperatures would produce emission peaks at longer wavelengths and the *JHK* flux from the cold dust might be lower than the detection limit.

The fit for the SED of LSQ13ddu at day 3.1 can be excluded since the derived temperatures for both two cases (2262 K and 2599 K) exceed 1900 K. The best-fit values of the masses derived from the SEDs of SN 2010al, the rest one SED of LSQ13ddu, and the SEDs of SN 2015G are $1.45 \times 10^{-5} M_{\odot}$, $5.9 \times 10^{-7} M_{\odot}$, and $2.4 \times 10^{-7} M_{\odot}$, respectively. The derived values of the masses of the dust associated with LSQ13ddu and SN 2015G are just the upper limits. While the possibility that there is a dust shell surrounding SN 2010al cannot be excluded, the derived mass of the dust associated with SN 2010al can also be regarded as an upper limit since, as mentioned above, the slight deviation from the data might be due to the fact that the simple blackbody model must produce smooth SEDs and the observed SEDs have undulation features. Hereafter, we only study the properties of the dust of OGLE-2012-SN-006.

3. DISCUSSION

3.1. Preexisting or New dust?

¹ <https://www.astro.princeton.edu/~draine/dust/dust.diel.html>

² Note that similar curves produced by Mie theory were shown in Figure 4 of Fox et al. (2010) for $a=0.001, 0.01, 0.10, \text{ and } 1.0 \mu\text{m}$ at the wavelength range between 10^{-2} and $\sim 10 \mu\text{m}$.

The NIR excesses of the SEDs can be produced by preexisting and/or new dust. To determine the nature of the dust of OGLE-2012-SN-006, a further analysis is needed. We first derived the luminosities of the SN photosphere (L_{ph}) and the dust (L_{d}), as well as the radius of the dust shell (R_{d}), based on the parameters listed in Table 3.

The luminosities of the SN photospheres and the dust shells can be respectively calculated by the equations

$$L_{\text{ph}} = 4\pi\sigma T_{\text{ph}}^4 R_{\text{ph}}^2, \quad (5)$$

and

$$L_{\text{d}} = 4\pi M_{\text{d}} \int_0^{\infty} B_{\nu}(T_{\text{d}}) \kappa_{\nu}(a) d\nu, \quad (6)$$

where $\sigma = 5.67 \times 10^{-5} \text{ erg cm}^{-2} \text{ K}^{-4}$ is the Stefan Boltzmann constant.

The lower limits of R_{d} at different epochs can be derived by the equation

$$R_{\text{bb}} = \left(\frac{L_{\text{d}}}{4\pi\sigma T_{\text{d}}^4} \right)^{1/2}. \quad (7)$$

As pointed by Fox et al. (2011), Equation (7) can only be used for an optically thick dust shell. For an optically thin dust shell, the value derived by Equation (7) is the lower limit of the radius of the dust shell, i.e., $R_{\text{d}} > R_{\text{bb}}$. The values of L_{ph} , L_{d} , and R_{d} of OGLE-2012-SN-006 are presented in Table 3.

By comparing Tables 2 and 3, we find that the radius of the SN photosphere of OGLE-2012-SN-006 at day 26.5 ($\sim 1.9 \times 10^{15} \text{ cm}$) is significantly smaller than the radius of the dust shell ($\gtrsim 6.8 \times 10^{16} \text{ cm}$) at the same epoch. At the early-time evolution, the radii of the surfaces of SN ejecta are slightly larger than that of the SN photospheres and we can assume that the two are approximately equal to each other. This result indicates that the radius of the dust shell surrounding OGLE-2012-SN-006 is significantly larger than that of the SN ejecta and the NIR excesses might be produced by the preexisting dust.

3.2. The Evolution of Some Parameters of OGLE-2012-SN-006

In Figure 4, we plot the evolution of the temperature, the radius, and the luminosity of the photosphere of OGLE-2012-SN-006 and the dust as well as the mass of the dust.

Throughout the evolution, the temperature of the SN photosphere of OGLE-2012-SN-006 is significantly higher than that of the dust, while the radius of the SN photosphere is significantly smaller than that of the dust shell; the luminosity of SN photosphere is lower than that of the dust shell, except for the epoch of day 151.6 when the SN photosphere luminosity is slightly higher than dust shell luminosity.

3.3. Comparison with Other Interacting SNe

Comparing the parameters of OGLE-2012-SN-006 with that of other interacting SNe (SNe Ibn and IIn) would provide us more information. Fox et al. (2011) used Spitzer to perform a survey for 68 nearby ($D < 250 \text{ Mpc}$) SNe IIn discovered between 1999 and 2008 and found that 10 events ($\sim 15\%$ of the sample) show late-time IR emission that can be explained by the emission of the dust. Fox et al. (2013) performed similar study for 10 SNe IIn discovered between 2005 and 2008, SN 2010jl, and seven other SNe. Here, we compare the parameters of OGLE-2012-SN-006 with that of the SNe IIn studied by Fox et al. (2011, 2013), and some SNe presented in other references.

In Figure 5, we plot the temperatures, radii, luminosities, and masses of the dust component of OGLE-2012-SN-006 at all epochs and these parameters of SN 2006jc (Mattila et al. 2008) as well as 16 type IIn SNe (SN 2005ip, Fox et al. 2009, 2013; SN 2005gn, SN 2008ip, SN 2008J, Fox et al. 2011; SN 2005cp, SN 2006jd, SN 2006qq, SN 2007rt, SN 2008cg, SN 2008en, SN 2008gm, Fox et al. 2011, 2013; SN 2005kd, SN 2008iy, Fox et al. 2013; SN 2010jl, Fox et al. 2013; Sarangi et al. 2018; SN 2015da, Tartaglia et al. 2020; SN 2006gy, Fox et al. 2013). By comparing the quantities of these SNe, one can get more interesting information.

The temperature of the dust of OGLE-2012-SN-006 is comparable to that of SNe 2006jc, 2005ip, 2010jl, and 2006gy at similar epochs, and higher than that of most of the SNe in the figure. This might be due to the fact that the IR data of the latter were obtained at late or very late epochs when the dust had cooled to lower temperatures.

The radius of the dust shell surrounding OGLE-2012-SN-006 is comparable to that of most of SNe in the figure and larger than that of SNe 2006jc, 2008gm, and 2008ip. As pointed out by Fox et al. (2011), the MIR emission of

the most SNe IIn (SN 2005cp, SN 2005gn, SN 2006jd, SN 2006qq, SN 2007rt, SN 2008cg, SN 2008en, SN 2008gm, SN 2008ip, and SN 2008J) in their sample was produced by preexisting dust. The fact that the radius of the dust shell of OGLE-2012-SN-006 is comparable to that of the SNe studied by Fox et al. (2011) provides further support to the conclusion that the NIR excesses of OGLE-2012-SN-006 might be produced by preexisting dust.

The luminosity of the dust of OGLE-2012-SN-006 is lower than that of SN 2006gy, which is a superluminous SN IIn, and its peak is more luminous than the luminosities of the dust of all other SNe in the figure.

The mass of the dust surrounding OGLE-2012-SN-006 is $\sim 0.5 - 2.0 \times 10^{-3} M_{\odot}$, about one magnitude lower than that of almost all SNe in the figure, but about one magnitude higher than that of SNe 2006jc and 2008gm.

4. CONCLUSION

It is widely believed that the IR excesses of SEDs of SNe might be produced by the preexisting and/or newly formed dust shells, so the early-time optical–NIR or late-time NIR/MIR SEDs of SNe would provide important clues for diagnosing the dust formation and make it possible to determine the physical properties of the dust associated with the ejecta and/or the progenitors of the SNe.

The aim of this paper is searching for the evidence of dust formation of SNe Ibn. To date, only six SNe Ibn have been observed in both optical and NIR bands. Prior to this study, two SNe Ibn (SN 2006jc and PS1-12sk) having NIR photometry have been researched. The optical–NIR SEDs of these two SNe Ibn exhibit different NIR features: SN 2006jc shows early-time NIR excesses that have been interpreted by the dust emission (Mattila et al. 2008), while the optical–NIR SEDs of PS1-12sk do not have evident IR excesses since its SEDs can be matched by the single-component blackbody model (Sanders et al. 2013). In this paper, we investigate the optical–NIR SEDs of four other Type Ibn SNe (SN 2010al, OGLE-2012-SN-006, LSQ13ddu, and SN 2015G) having optical–NIR photometry.

By using the single-component blackbody model, we find that the SEDs of SN 2010al, LSQ13ddu, and SN 2015G can be well explained by the model. The results indicate that the evidence of the significant dust formation associated with these three SNe is absent. In contrast, the optical–NIR SEDs of OGLE-2012-SN-006 cannot be reproduced by the single-component blackbody model and the NIR excesses of the SEDs of OGLE-2012-SN-006 are obvious.

Therefore, we invoke the double-component model assuming that the SEDs were produced by the SN photosphere and the heated dust to fit the SEDs of OGLE-2012-SN-006 at different epochs. To get the upper limits of the masses of the dust of SN 2010al, LSQ13ddu, and SN 2015G, we also employ this model to fit their optical–NIR SEDs.

We find that the IR excesses of the SEDs of OGLE-2012-SN-006 can be interpreted by the double-component model. The best-fitting temperatures of the two classes of dust (graphite and silicate) at different epochs favor the graphite dust, and the derived mass and temperature of the graphite dust are $\sim 0.5 - 2.0 \times 10^{-3} M_{\odot}$ and $\sim 1200 - 1300$ K, respectively. This indicates that OGLE-2012-SN-006 is the another SN Ibn showing evidence of the dust formation. On the other hand, our fits for the SEDs of SN 2010al, LSQ13ddu, and SN 2015G suggest that the upper limits of masses of possible dust of these three SNe Ibn are $1.45 \times 10^{-5} M_{\odot}$, $5.9 \times 10^{-7} M_{\odot}$, and $2.4 \times 10^{-7} M_{\odot}$, respectively.

A further analysis for the dust of OGLE-2012-SN-006 suggests that the radius of the optically thin dust shell is $\sim 6.8 \times 10^{16}$ cm which is significantly larger than the radius of the SN ejecta at day 26.5 ($\sim 1.9 \times 10^{15}$ cm), indicating that the dust shell is preexisting one.

We compare the temperature, the radii, the luminosity, as well as the mass of the dust shell of OGLE-2012-SN-006 to that of SN 2006jc and 16 SNe IIn (SN 2005cp, SN 2005gn, SN 2005ip, SN 2005kd, SN 2006gy, SN 2006jd, SN 2006qq, SN 2007rt, SN 2008cg, SN 2008en, SN 2008gm, SN 2008ip, SN 2008iy, SN 2008J, SN 2010jl, and SN 2015da), finding some additional information. The temperature of the dust of OGLE-2012-SN-006 is comparable to that of SNe 2006jc, 2005ip, 2010jl, and 2006gy, and higher than that of most of the 17 SNe; the radius of the dust shell of OGLE-2012-SN-006 is comparable to that of most SNe IIn and larger than that of SN 2006jc, SN 2008gm, and 2008ip; the peak luminosity of the dust of OGLE-2012-SN-006 is higher than the luminosities of the dust of all other SNe, except for that of SN 2006gy; the mass of the dust of OGLE-2012-SN-006 ($\sim 10^{-3} M_{\odot}$) is about 1/10 times that of most SNe IIn in the sample, but about 10 times that of SNe 2006jc and 2008gm.

According to the fits for the SEDs of two SNe Ibn (SN 2006jc and PS1-12sk) having optical–NIR photometry coverage, one might infer that the percentage of SNe Ibn having IR excesses produced by the heated dust is 50%. However, the sample containing only two events was too small, making it impossible to get a valid conclusion. Our

study, together with the previous studies, indicates that at least about 1/3 of SNe Ibn show evidence for dust formation.³

We caution, however, that the sample we collect is still rather small. The future optical and IR observations for more SNe Ibn would provide a larger sample, making it possible to perform a systematic study for the dust formation of SNe Ibn and get a stronger conclusion about the ratio of the SNe Ibn with significant dust formation to all SNe Ibn.

ACKNOWLEDGMENTS

We thank the anonymous referee for helpful comments and suggestions that have allowed us to improve this manuscript. This work is supported by National Natural Science Foundation of China (grants 11963001, 11533003, 11603006, 11673006, 11851304, 11973020 (C0035736), U1731239, and U1938201), Guangxi Science Foundation (grants 2016GXNSFCB380005, 2016GXNSFFA380006, and 2017GXNSFFA198008, AD17129006, 2018GXNSFGA281007, 2019JJD110006, and 2019AC20334), and the Bagui Young Scholars Program (LHJ).

³ We caution that this fraction is approximate (because it is based on a small sample size of six) and should be regarded as a lower limit (since the evidence of the dust formation of many SNe was found by analyzing the late-time observations, while all the SNe Ibn we study lack late-time observations.)

REFERENCES

- Clark, P., Maguire, K., Inserra, C., et al. 2020, MNRAS, 492, 2208
- Draine, B. T., & Lee, H. M. 1984, ApJ, 285, 89
- Draine, B.T. 2003, ApJ, 598, 1026
- Dwek, E. 1983, ApJ, 274, 175
- Dwek, E. 1985, ApJ, 297, 719
- Foreman-Mackey, D., Hogg, D. W., Lang, D., et al. 2013, PASP, 125, 306
- Foley, R. J., Smith, N., Ganeshalingam, M., et al. 2007, ApJL, 657, L105
- Fox, O. D., Chevalier, R. A., Dwek, E., et al. 2010, ApJ, 725, 1768
- Fox, O. D., Chevalier, R. A., Skrutskie, M. F., et al. 2011, ApJ, 741, 7
- Fox, O. D., Skrutskie, M. F., Chevalier, R. A., et al. 2009, ApJ, 691, 650
- Fox, O. D., Filippenko, A. V., Skrutskie, M. F., Silverman, J. M., Ganeshalingam, M., Cenko, S. B., & Clubb, K. I. 2013, AJ, 146, 2
- Gall, C., Hjorth, J., Watson, D., et al. 2014, Nature, 511, 326
- Hildebrand, R. H. 1983, QJRAS, 24, 267
- Hossein-zadeh, G., Arcavi, I., Valenti, S., et al. 2017, ApJ, 836, 158
- Hossein-zadeh, G., McCully, C., Zabludoff, A. I., et al. 2019, ApJL, 871, L9
- Laor, A., & Draine, B. T. 1993, ApJ, 402, 441
- Mattila, S., Meikle, W. P. S., Lundqvist, P., et al. 2008, MNRAS, 389, 141
- Pastorello, A., Mattila, S., Zampieri, L., et al. 2008, MNRAS, 389, 113
- Pastorello, A., Benetti, S., Brown, P. J., et al. 2015a, MNRAS, 449, 1921
- Pastorello, A., Smartt, S. J., Mattila, S., et al. 2007, Nature, 447, 829
- Pastorello, A., Wang, X.-F., Ciabattari, F., et al. 2016, MNRAS, 456, 853
- Pastorello, A., Wyrzykowski, Ł., Valenti, S., et al. 2015b, MNRAS, 449, 1941
- Sanders, N. E., Soderberg, A. M., Foley, R. J., et al. 2013, ApJ, 769, 39
- Sarangi, A., Dwek, E., & Arendt R. G. 2018, ApJ, 859, 66
- Shivvers, I., Zheng, W., Van Dyk, S. D., et al. 2017, MNRAS, 471, 4381
- Smith, N., Foley, R. J., & Filippenko, A. V. 2008, ApJ, 680, 568
- Stritzinger, M., Taddia, F., Fransson, C., et al. 2012, ApJ, 756, 173
- Szalai, T., Zsíros, S., Fox, O. D., Pejcha, O., & Müller, T. 2019, ApJS, 241, 38
- Tartaglia, L., Pastorello, A., Sollerman, J., et al. 2020, A&A, 635A, 39
- Tominaga, N., Limongi, M., Suzuki, T., et al. 2008, ApJ, 687, 1208

Table 1. The information on the SNe in the sample

Name	R.A. (J2000)	Decl. (J2000)	Redshift	Discovery Date	Obs. Filters	References ^a
SN 2010al	08 ^h 14 ^m 15 ^s .91	+18°2′18″.2	0.017	Mar 13.03 2010	UVOT filters ^b , <i>U, B, V, R, I, J, H, K_s</i>	1
OGLE-2012-SN-006	03 ^h 33 ^m 34 ^s .79	−74°2′40″.1	0.06	Oct 7.34 2012	<i>U, B, V, R, I, J, H, K_s</i>	2
LSQ13ddu	03 ^h 58 ^m 49 ^s .09	+29°2′11″.8	0.058	Nov 26.3 2013	UVOT filters ^b , <i>U, B, V, g, r, i, z, Y, J, H, K_s</i>	3
SN 2015G	20 ^h 37 ^m 25 ^s .58	+66°2′11″.5	0.005	Mar 23.78 2015	<i>B, V, R, I, J, H, K_s</i>	4

^a References: (1) Pastorello et al. (2015a); (2) Pastorello et al. (2015b); (3) Clark et al. (2020); (4) Shivvers et al. (2017).

^b *uvw2, uvm2, uvw1, u, b, and v.*

Table 2. The best-fitting parameters of the Blackbody plus Graphite (Silicate) model for the SEDs of the four SNe Ibn at the different rest-frame epochs.

Phase ^a	Blackbody plus Graphite					Blackbody plus Silicate				
	T_{ph} (K)	R_{ph} (10^{15} cm)	T_{d} (K)	M_{d} ($10^{-6}M_{\odot}$)	χ^2/dof	T_{ph} (K)	R_{ph} (10^{15} cm)	T_{d} (K)	M_{d} ($10^{-6}M_{\odot}$)	χ^2/dof
SN 2010al										
11.3 d	13666.97 ^{+625.6} _{-520.7}	0.9 ^{+0.1} _{-0.1}	521.75 ^{+1251.8} _{-351.9}	1.79 ^{+854.8} _{-1.8}	2.88	13648.11 ^{+599.3} _{-512.0}	0.9 ^{+0.1} _{-0.1}	555.96 ^{+1270.2} _{-380.0}	2.79 ^{+1250.4} _{-2.8}	2.87
12.3 d	10504.2 ^{+1319.3} _{-1119.4}	1.25 ^{+0.3} _{-0.2}	1651.93 ^{+484.4} _{-869.1}	14.53 ^{+67.9} _{-10.6}	0.76	10576.04 ^{+1619.4} _{-1214.4}	1.23 ^{+0.3} _{-0.2}	2010.38 ^{+693.6} _{-1100.0}	83.62 ^{+272.4} _{-55.2}	0.96
14.3 d	10025.75 ^{+531.8} _{-459.4}	1.35 ^{+0.1} _{-0.1}	639.69 ^{+1099.0} _{-451.8}	4.27 ^{+1021.6} _{-4.3}	2.15	10042.15 ^{+522.3} _{-455.8}	1.35 ^{+0.1} _{-0.1}	714.51 ^{+1224.4} _{-524.0}	16.06 ^{+1830.1} _{-16.1}	2.11
16.2 d	9730.24 ^{+193.0} _{-188.6}	1.41 ^{+0.1} _{-0.1}	452.65 ^{+1139.4} _{-289.7}	0.72 ^{+497.3} _{-0.7}	0.69	9731.01 ^{+184.9} _{-178.4}	1.41 ^{+0.1} _{-0.1}	479.14 ^{+1097.3} _{-314.4}	1.06 ^{+710.4} _{-1.1}	0.68
23.0 d	7667.52 ^{+119.4} _{-122.4}	1.82 ^{+0.1} _{-0.1}	394.65 ^{+835.8} _{-240.7}	0.41 ^{+680.2} _{-0.4}	2.08	7667.84 ^{+121.4} _{-122.3}	1.83 ^{+0.1} _{-0.1}	449.84 ^{+967.8} _{-287.1}	0.77 ^{+786.4} _{-0.8}	2.08
26.0 d	7263.98 ^{+119.3} _{-126.0}	1.8 ^{+0.1} _{-0.1}	439.33 ^{+826.7} _{-278.2}	0.85 ^{+1165.2} _{-0.9}	2.87	7265.26 ^{+119.9} _{-118.7}	1.8 ^{+0.1} _{-0.1}	474.91 ^{+893.0} _{-311.3}	1.25 ^{+1500.4} _{-1.2}	2.87
29.8 d	6786.31 ^{+129.9} _{-130.3}	1.73 ^{+0.1} _{-0.1}	378.14 ^{+822.4} _{-226.6}	0.31 ^{+557.1} _{-0.3}	1.66	6786.59 ^{+130.1} _{-130.5}	1.73 ^{+0.1} _{-0.1}	424.24 ^{+921.3} _{-264.6}	0.64 ^{+756.0} _{-0.6}	1.66
37.0 d	6467.84 ^{+153.6} _{-152.3}	1.21 ^{+0.1} _{-0.1}	369.78 ^{+812.5} _{-217.6}	0.24 ^{+558.2} _{-0.4}	1.49	6463.44 ^{+151.6} _{-151.5}	1.21 ^{+0.1} _{-0.1}	404.2 ^{+917.2} _{-246.7}	0.49 ^{+678.2} _{-0.5}	1.49
40.7 d	6215.12 ^{+249.2} _{-241.7}	1.05 ^{+0.1} _{-0.1}	384.93 ^{+883.8} _{-231.2}	0.36 ^{+563.9} _{-0.4}	0.36	6216.45 ^{+242.3} _{-243.8}	1.05 ^{+0.1} _{-0.1}	431.94 ^{+1006.5} _{-272.4}	0.58 ^{+667.5} _{-0.6}	0.36
43.6 d	6193.35 ^{+363.7} _{-377.9}	0.9 ^{+0.1} _{-0.1}	404.42 ^{+903.8} _{-248.6}	0.43 ^{+765.8} _{-0.4}	0.64	6201.26 ^{+356.7} _{-379.5}	0.9 ^{+0.1} _{-0.1}	446.64 ^{+998.5} _{-284.3}	0.93 ^{+992.6} _{-0.9}	0.64
59.5 d	6069.16 ^{+218.2} _{-202.6}	0.37 ^{+0.0} _{-0.0}	1141.56 ^{+216.4} _{-254.8}	7.88 ^{+33.2} _{-5.1}	3.04	6070.44 ^{+242.0} _{-204.0}	0.37 ^{+0.0} _{-0.0}	1329.58 ^{+292.0} _{-318.6}	40.51 ^{+150.6} _{-25.8}	3.12
OGLE-2012-SN-006										
26.5 d	7783.53 ^{+475.4} _{-419.3}	1.92 ^{+0.2} _{-0.2}	1312.57 ^{+47.3} _{-47.6}	1963.09 ^{+593.9} _{-441.8}	1.62	7986.53 ^{+541.6} _{-524.4}	1.83 ^{+0.2} _{-0.2}	1505.2 ^{+61.2} _{-66.7}	12810.53 ^{+3613.9} _{-3037.9}	1.91
111.1 d	6504.53 ^{+306.2} _{-290.3}	1.6 ^{+0.1} _{-0.1}	1243.17 ^{+42.7} _{-41.0}	1456.3 ^{+406.0} _{-321.1}	3.74	6688.26 ^{+364.1} _{-347.4}	1.49 ^{+0.2} _{-0.1}	1456.82 ^{+59.2} _{-58.3}	7987.22 ^{+2188.0} _{-1810.3}	2.61
120.6 d	6541.24 ^{+263.3} _{-246.1}	1.55 ^{+0.1} _{-0.1}	1204.05 ^{+57.2} _{-54.9}	1502.76 ^{+599.3} _{-428.7}	3.57	6659.75 ^{+300.4} _{-271.1}	1.49 ^{+0.1} _{-0.1}	1417.71 ^{+78.9} _{-74.5}	7821.45 ^{+3119.6} _{-2207.8}	2.79
133.9 d	7144.95 ^{+253.9} _{-237.9}	1.28 ^{+0.1} _{-0.1}	1294.96 ^{+66.0} _{-60.2}	747.98 ^{+319.2} _{-229.8}	3.9	7369.76 ^{+346.9} _{-293.0}	1.2 ^{+0.1} _{-0.1}	1515.52 ^{+86.5} _{-80.2}	4346.93 ^{+1768.7} _{-1266.1}	3.55
151.6 d	7974.58 ^{+431.7} _{-391.2}	0.95 ^{+0.1} _{-0.1}	1303.87 ^{+68.7} _{-66.5}	479.87 ^{+214.3} _{-145.3}	17.29	8116.14 ^{+471.8} _{-420.5}	0.92 ^{+0.1} _{-0.1}	1520.6 ^{+86.6} _{-82.0}	2889.66 ^{+1165.1} _{-813.6}	15.6
179.9 d	7208.97 ^{+430.4} _{-392.0}	0.91 ^{+0.1} _{-0.1}	1219.67 ^{+72.6} _{-69.4}	673.45 ^{+357.6} _{-228.9}	7.32	7346.22 ^{+482.6} _{-411.5}	0.88 ^{+0.1} _{-0.1}	1436.77 ^{+95.1} _{-91.3}	3551.44 ^{+1777.3} _{-1140.6}	6.24
185.6 d	6428.12 ^{+418.3} _{-391.8}	1.07 ^{+0.1} _{-0.1}	1256.21 ^{+53.6} _{-52.1}	525.17 ^{+189.1} _{-135.0}	9.91	6609.77 ^{+465.1} _{-462.5}	1.0 ^{+0.2} _{-0.1}	1477.91 ^{+74.5} _{-74.7}	2828.39 ^{+993.5} _{-761.4}	7.95
LSQ13ddu										
3.1 d	50540.99 ^{+6570.7} _{-5253.3}	0.42 ^{+0.0} _{-0.0}	2262.37 ^{+62.8} _{-62.9}	10.54 ^{+1.5} _{-1.4}	55.74	55602.67 ^{+10430.9} _{-7489.6}	0.39 ^{+0.0} _{-0.0}	2599.33 ^{+86.4} _{-90.3}	111.44 ^{+15.8} _{-13.9}	67.72
14.5 d	8067.59 ^{+276.9} _{-191.7}	1.56 ^{+0.1} _{-0.1}	449.84 ^{+1941.9} _{-288.3}	0.59 ^{+257.7} _{-0.6}	3.93	8037.6 ^{+189.7} _{-176.9}	1.57 ^{+0.1} _{-0.1}	414.05 ^{+990.7} _{-255.6}	0.53 ^{+611.5} _{-0.5}	3.92
SN 2015G										
42.3 d	6837.98 ^{+214.6} _{-212.7}	0.44 ^{+0.0} _{-0.0}	302.12 ^{+561.0} _{-159.3}	0.14 ^{+482.0} _{-0.1}	13.96	6836.47 ^{+216.0} _{-213.2}	0.44 ^{+0.0} _{-0.0}	331.73 ^{+634.4} _{-184.9}	0.24 ^{+504.1} _{-0.2}	13.96
59.2 d	6317.11 ^{+228.1} _{-230.1}	0.36 ^{+0.0} _{-0.0}	305.74 ^{+660.9} _{-162.5}	0.11 ^{+415.1} _{-0.1}	7.11	6312.44 ^{+229.9} _{-225.6}	0.36 ^{+0.0} _{-0.0}	327.27 ^{+645.9} _{-180.9}	0.21 ^{+507.0} _{-0.2}	7.1

Note. Here, T_{ph} is the temperature of the SN photosphere, R_{ph} is the radius of the SN photosphere, T_{d} is the temperature of the dust shell, and M_{d} is the mass of the dust shell.

^a All the phases are relative to the possible corresponding explosion days that are supposed to be respectively JD 2455268 (SN 2010al), JD 2456203.8 (OGLE-2012-SN-006), JD 2457080.5 (SN 2015G), and JD 2456621.4 (LSQ13ddu).

Table 3. The derived values of the SN photosphere luminosities (L_{ph}), the dust luminosities (L_{d}), and the lower limits of the radii (R_{d}) of the dust shell surrounding OGLE-2012-SN-006 at different epochs.

Phase (days)	L_{ph} (10^{42} erg s^{-1})	L_{d} (10^{42} erg s^{-1})	R_{d} (10^{16} cm)
26.5	$9.65^{+0.5}_{-0.4}$	$9.87^{+0.6}_{-0.6}$	$> 6.83^{+0.7}_{-0.6}$
111.1	$3.25^{+0.1}_{-0.1}$	$5.29^{+0.3}_{-0.3}$	$> 5.57^{+0.5}_{-0.5}$
120.6	$3.16^{+0.1}_{-0.1}$	$4.51^{+0.4}_{-0.4}$	$> 5.49^{+0.7}_{-0.6}$
133.9	$3.03^{+0.1}_{-0.1}$	$3.47^{+0.4}_{-0.3}$	$> 4.16^{+0.6}_{-0.5}$
151.6	$2.6^{+0.1}_{-0.1}$	$2.32^{+0.2}_{-0.2}$	$> 3.35^{+0.5}_{-0.4}$
179.9	$1.62^{+0.1}_{-0.0}$	$2.19^{+0.2}_{-0.2}$	$> 3.72^{+0.6}_{-0.5}$
185.6	$1.39^{+0.0}_{-0.0}$	$2.03^{+0.1}_{-0.1}$	$> 3.38^{+0.4}_{-0.3}$

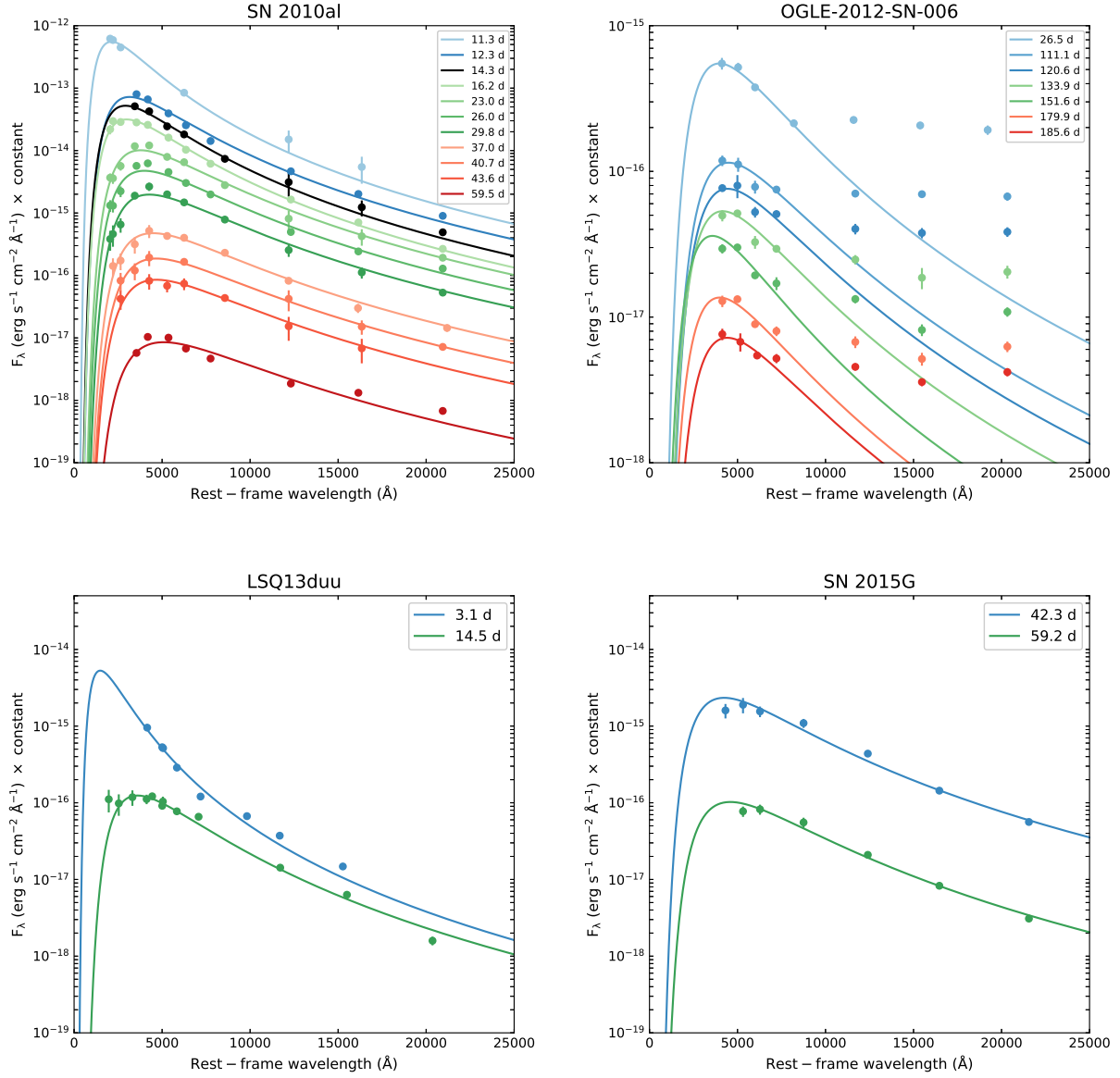


Figure 1. The optical and NIR SEDs of SN 2010al, OGLE-2012-SN-006, LSQ13duu, and SN 2015G and the fits of the single-component blackbody model. The data are from the references listed in Table 1. For clarity, the flux at all epochs are shifted by adding different constants.

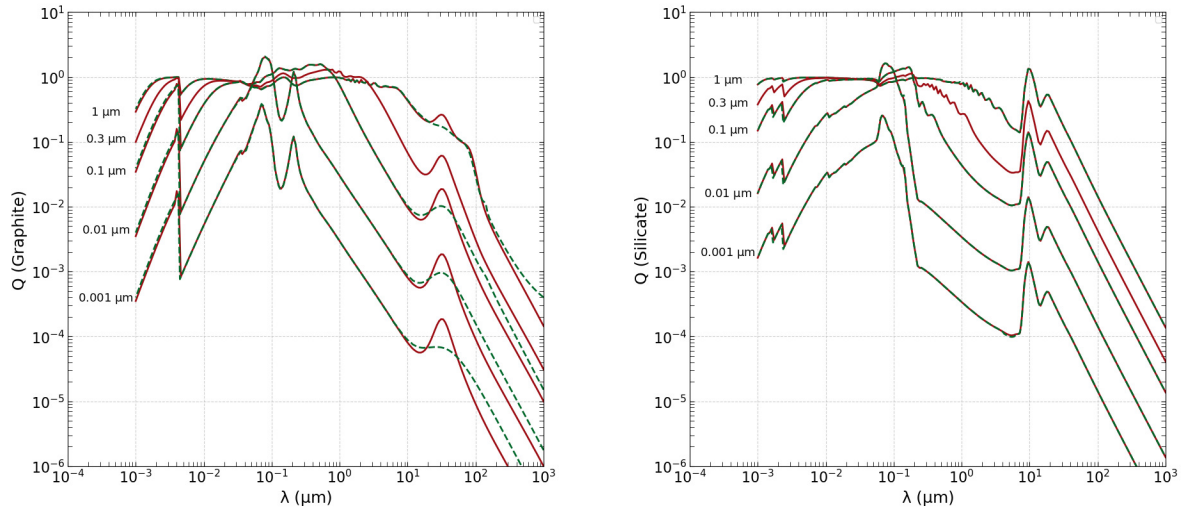


Figure 2. The emission efficiencies ($Q_{\nu}(a)$) for graphite (left panel) and silicate (right panel) for $a=0.001, 0.01, 0.10, 0.3,$ and $1.0 \mu\text{m}$. The solid lines present the curves we calculated using Mie theory, while the dashed lines present the curves yielded by the data obtained from Draine's website. Note that the dashed line corresponding the case of $a = 0.3 \mu\text{m}$ is absent since the website provide no data for this case.

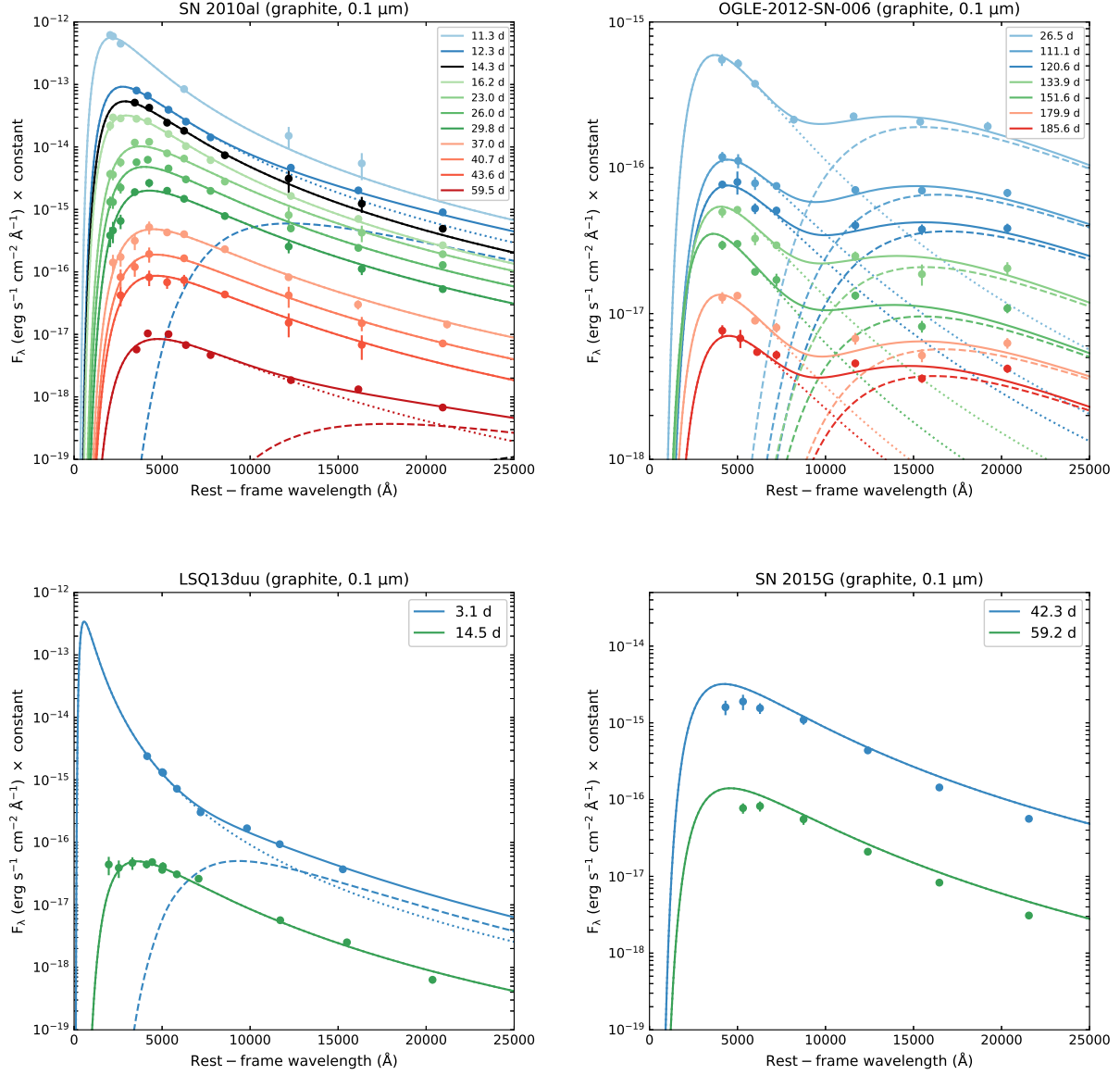


Figure 3. The best-fitting SEDs of SN 2010al, OGLE-2012-SN-006, LSQ13ddu, and SN 2015G obtained by using the two-component model. The dotted, the dashed, and the solid lines present the flux of SN photospheres, dust, and the sum of the two components, respectively. The data are from the references listed in Table 1. For clarity, the plots at all epochs have been shifted vertically.

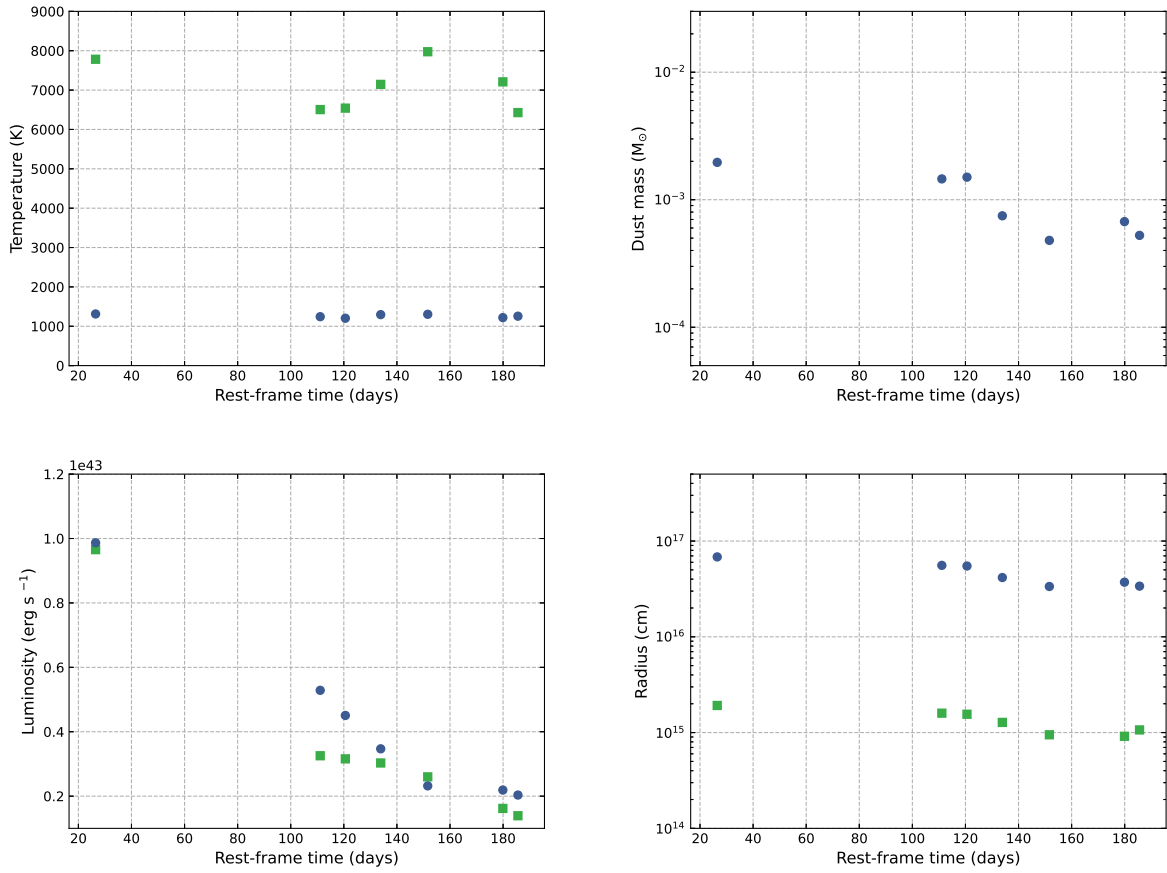


Figure 4. The evolution of the temperatures (the top-left panel), the dust masses (the top-right panel), the luminosities of the SN photosphere and the dust (the bottom-left panel), and the radii (the bottom-right panel) of OGLE-2012-SN-006.

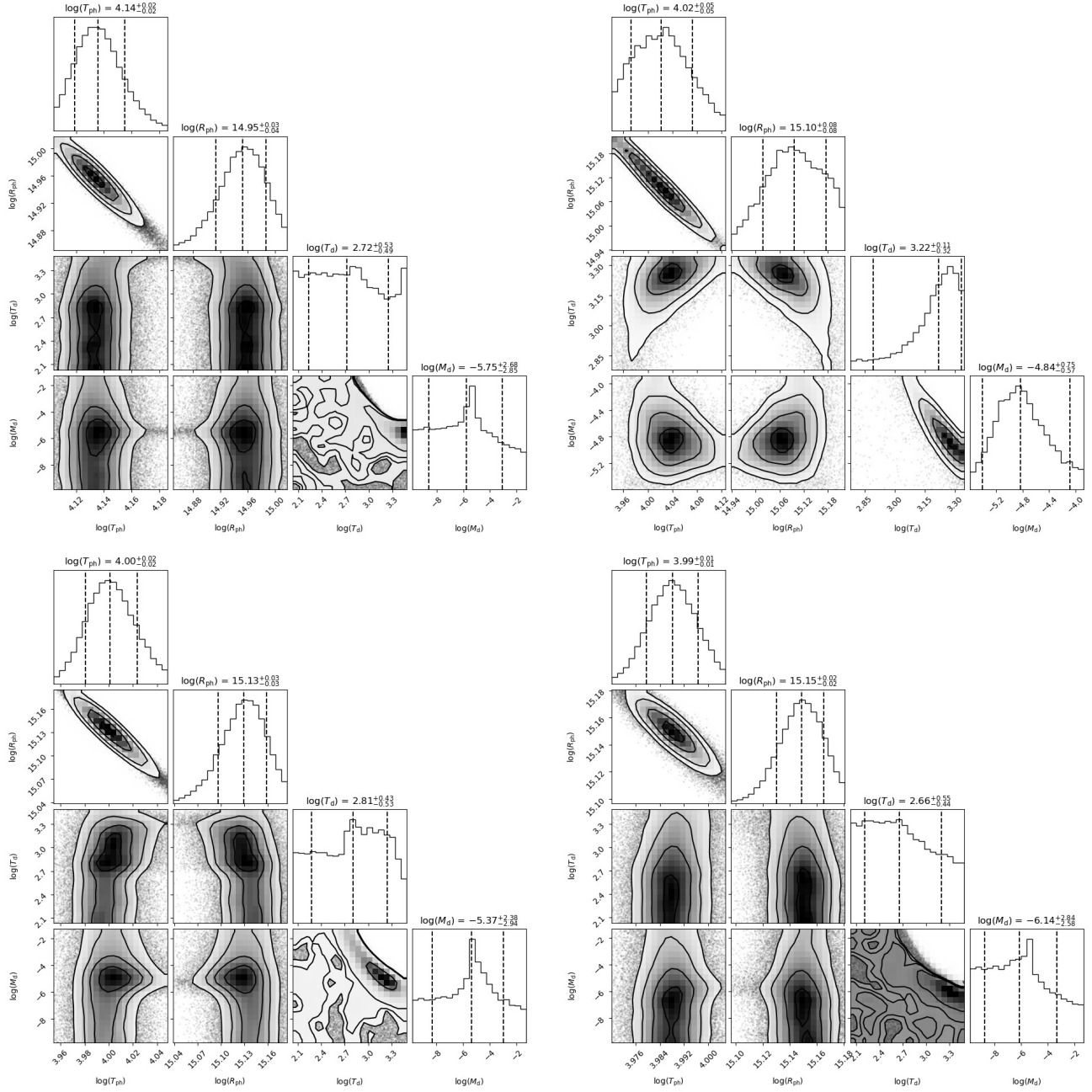


Figure A1. The corner plots of the two-component model for SEDs of SN 2010al.

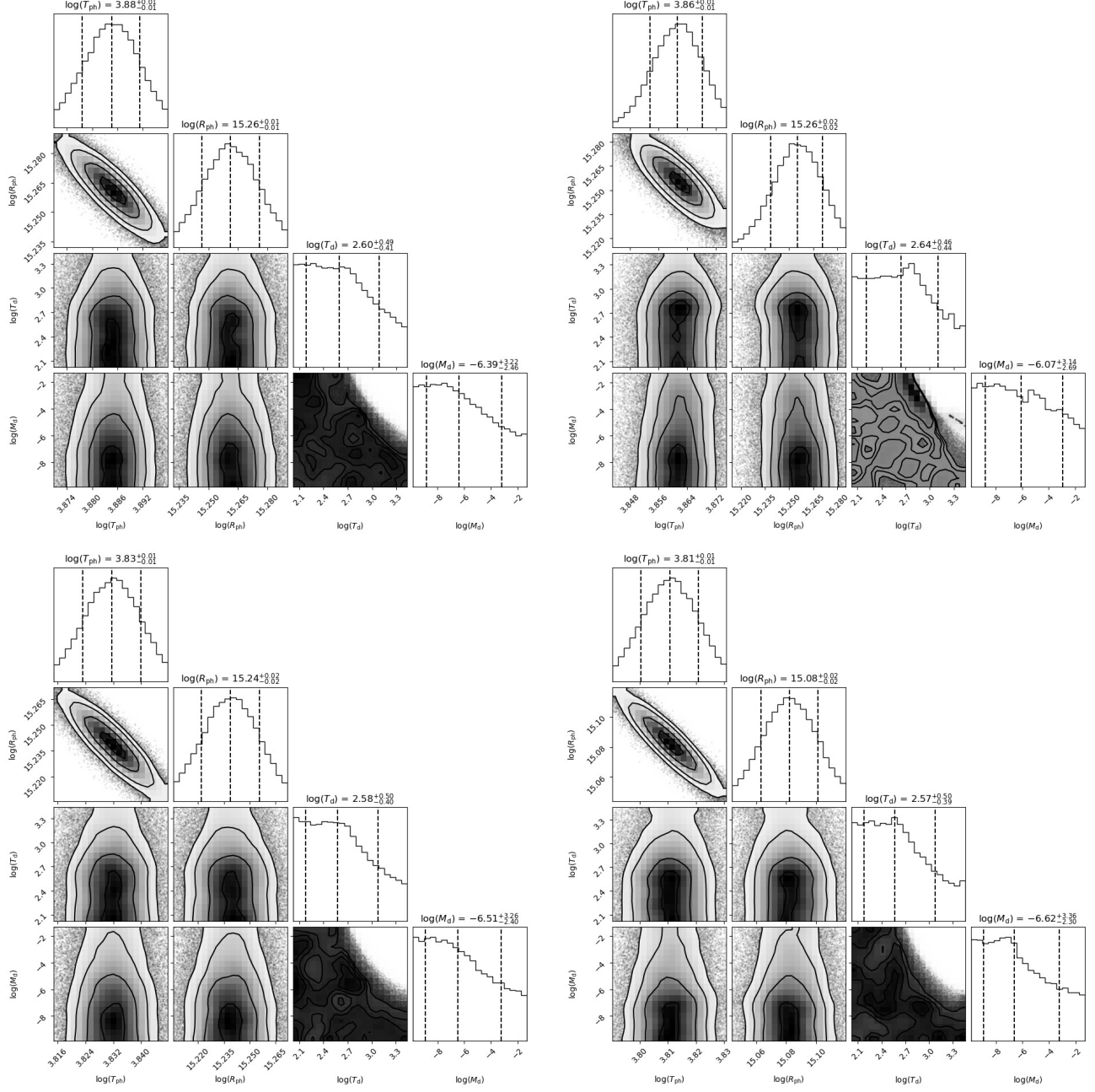


Figure A1. The corner plots of the two-component model for SEDs of SN 2010al—continued.

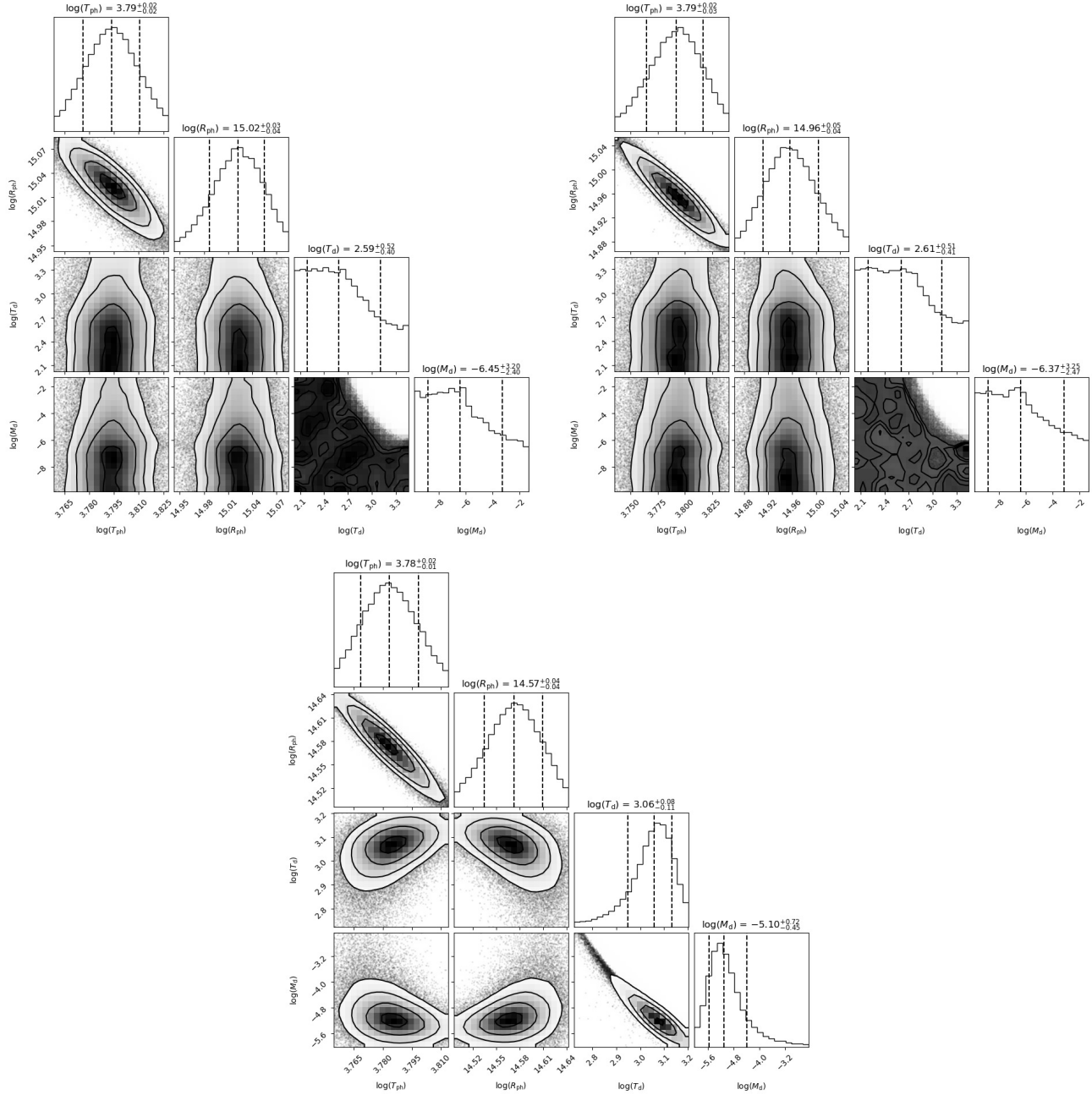


Figure A1. The corner plots of the two-component model for SEDs of SN 2010al—continued.

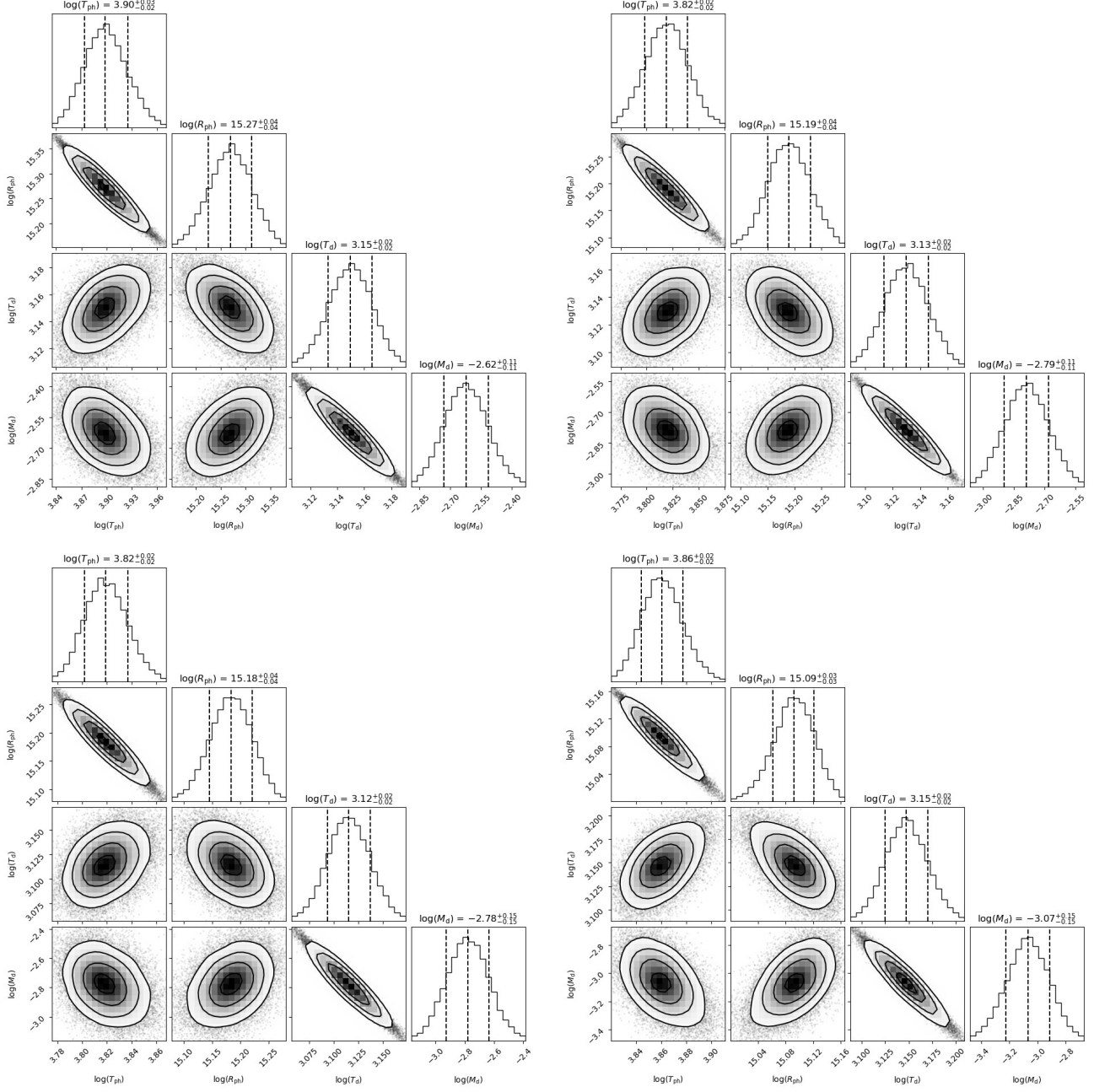


Figure A2. The corner plots of the two-component model for SEDs of OGLE-2012-SN-006.

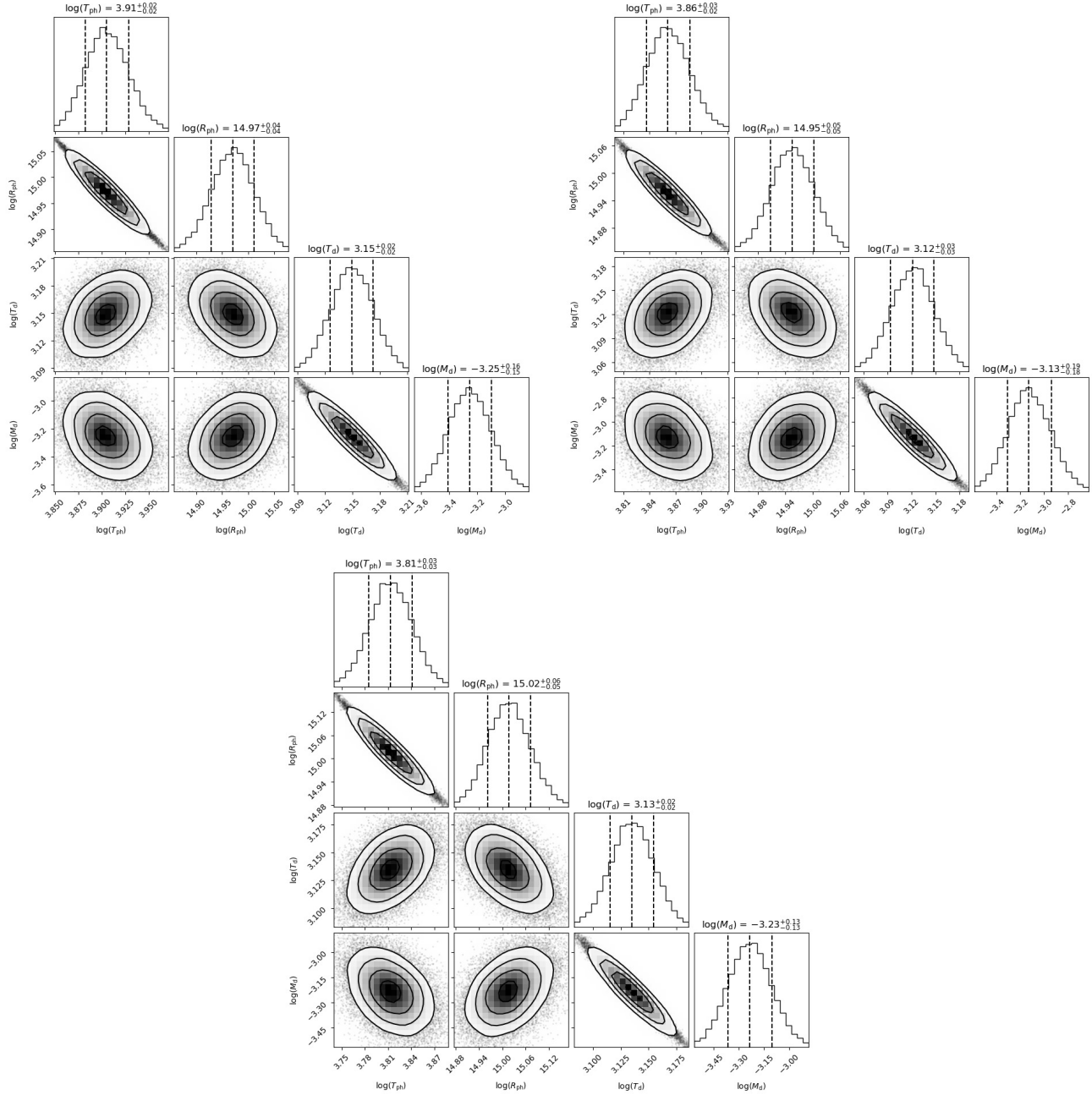


Figure A2. The corner plots of the two-component model for SEDs of OGLE-2012-SN-006—continued.

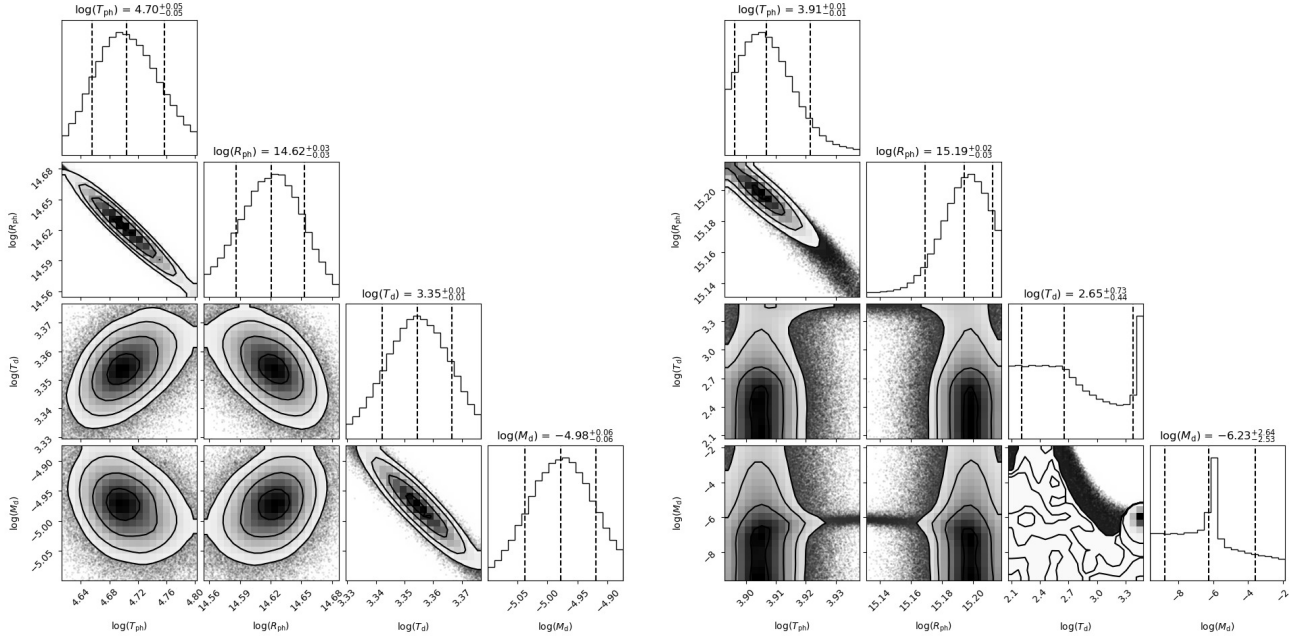


Figure A3. The corner plots of the two-component model for SEDs of LSQ13ddu.

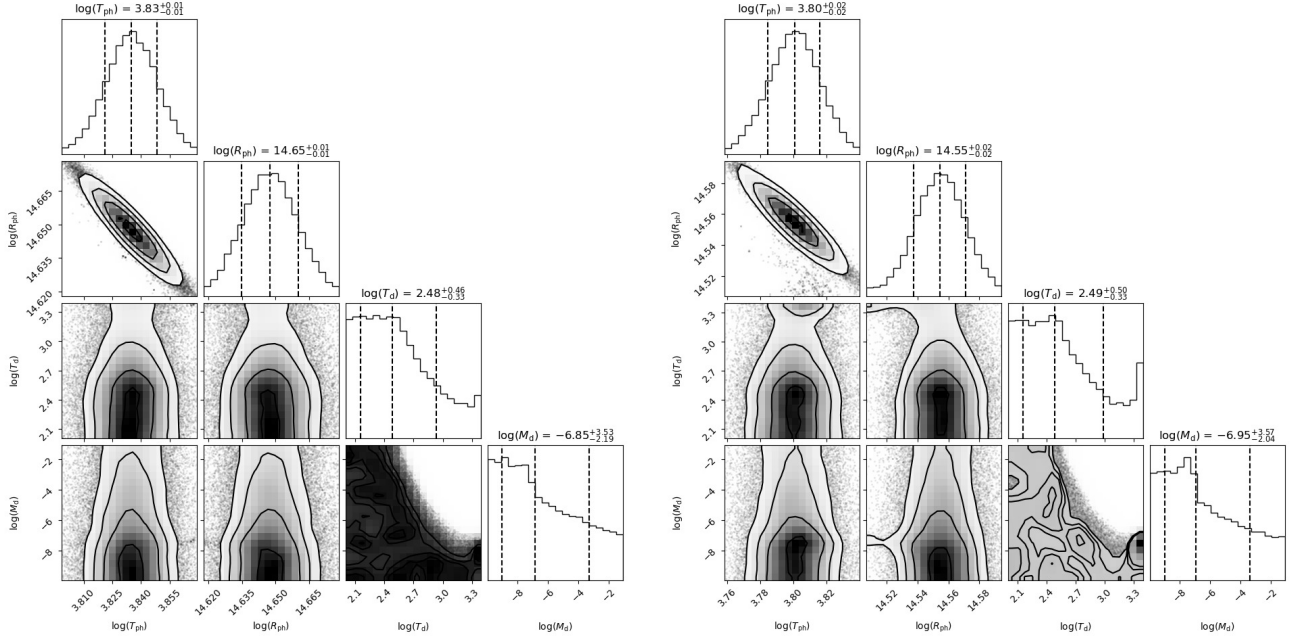


Figure A4. The corner plots of the two-component model for SEDs of SN 2015G.